# Supra-Monolayer Coverages on Small Metal Clusters and Their Effects on H$_2$ Chemisorption Particle Size Estimates

**Abdulrahman S. Almithn and David D. Hibbitts**
Dept. of Chemical Engineering, University of Florida, Gainesville, FL 32611

*H$_2$ chemisorption measurements are used to estimate the size of supported metal particles, often using a hydrogen-to-surface-metal stoichiometry of unity. This technique is most useful for small particles whose sizes are difficult to estimate through electron microscopy or X-ray diffraction. Undercoordinated metal atoms at the edges and corners of particles, however, make up large fractions of small metal clusters, and can accommodate multiple hydrogen atoms leading to coverages which exceed 1 ML (supra-monolayer). Density functional theory was used to calculate hydrogen adsorption energies on Pt and Ir particles (38–586 atoms, 0.8–2.4 nm) at high coverages ($\leq$3.63 ML). Calculated differential binding energies confirm that Pt and Ir (111) single-crystal surfaces saturate at 1 ML; however, Pt and Ir clusters saturate at supra-monolayer coverages as large as 2.9 ML. Correlations between particle size and saturation coverage are provided that improve particle size estimates from H$_2$ chemisorption for Pt-group metals.* © 2018 American Institute of Chemical Engineers *AIChE J*, 64: 3109–3120, 2018
*Keywords: density functional theory, chemisorption, coverage effects, coadsorbate interactions, transition metals*

## Introduction

Noble metal catalysts are used extensively for many thermo-, electro-, and photochemical reactions, including hydrogenation, dehydrogenation, and oxidation of hydrocarbons,[1–5] CO oxidation and hydrogenation,[6,7] oxygen reduction on anode surfaces,[8] and light-induced H$_2$ evolution.[9] The size of the supported metal particles of these catalysts has a significant impact on process economics because only surface metal atoms can interact with reagents. Previous studies show that metal particles size has a significant effect on coke formation and catalytic deactivation during reforming processes.[10,11] Furthermore, particle size can have an impact on the rate per surface metal atom (turnover rate) for "structure-sensitive" reactions;[12,13] metal particles of different sizes expose surface ensembles with unique structures. Therefore, accurate assessment of the size of supported metal particle catalysts is critical for characterization of these materials.

Molecular hydrogen (H$_2$) is a common reagent in metal-catalyzed reactions, such as the hydrogenation of unsaturated C $=$ C bonds[14] and the reduction of CO,[15,16] NO,[17,18] or N$_2$;[19,20] it is also used to cleave C–C bonds in alkane hydrogenolysis,[21–27] C–O bonds in hydrodeoxygenation,[28,29] and C–S bonds in hydrodesulfurization.[30] H$_2$ readily dissociates on most noble metal catalysts, including Pt and Ir,[31,32] at ambient or near-ambient conditions. Dissociative chemisorption of H$_2$ has therefore been widely used as a chemical titration to estimate the dispersion of supported metal particles, which is the fraction of metal atoms present at particle surfaces and therefore accessible to reagents.[33–37] H$_2$ isotherms are generated to determine the amount of strongly bound (chemisorbed) H* adsorbed at "saturation" (the H* coverage in equilibrium with the highest pressure used in the isotherms) while excluding weakly bound (physisorbed) H$_2$. Metal dispersions are then calculated by assuming a H* to surface-metal (H:M$_s$) stoichiometry at saturation ($\theta_{sat}$, often assumed to be unity), and particle sizes can be estimated from dispersion for a given particle shape (e.g., hemispherical, spherical). X-ray diffraction (XRD) and transmission electron microscopy (TEM) can confirm these particle size estimates; however, small metal particles ($<$1 nm in diameter) are difficult to observe in standard TEM instruments and their sizes are inaccurately estimated using XRD.[34,38,39] For these highly dispersed noble metal catalysts, the most common estimate of their size is given by H$_2$ chemisorption,[34,35] which requires an accurate estimate of saturation H* coverages during chemisorption experiments.

Surface science studies suggest $\theta_{sat}$ values of unity on the (111) plane of FCC metal crystals (such as Ir and Pt) at H$_2$ chemisorption conditions.[31,40] The (111) plane represents $>$90% of the surface of large metal particles ($>$4 nm) and, therefore, the assumption that $\theta_{sat}$ is unity is reasonable for large particles. The Brunauer-Emmett-Teller (BET)[41] method has been used to estimate the H:M$_s$ stoichiometry for unsupported metal particles by measuring the monolayer volume of an inert gas (e.g., N$_2$) physisorbed on the surface. Spenadel and Boudart[42] found that the surface area measured from H$_2$ chemisorption on unsupported platinum particles (430 nm) agrees well with its BET surface area and concluded that H:Pt$_s$ is indeed unity; however, these particles are $\sim$100 times larger

than those typical of supported catalysts. Other studies used electron microscopy and small angle X-ray diffraction to measure the particles dispersion independently and also confirmed a $\theta_{sat}$ of unity for particles >5 nm in diameter.[35–37,42–44] Average particle sizes calculated from $H_2$ chemisorption on Ir/$Al_2O_3$ by assuming $\theta_{sat}$ of 1 (2.2 nm) were slightly smaller than the average size observed directly by TEM (2.9 nm).[45] Values of unity for $\theta_{sat}$ are often assumed, based on these studies, for other metals that are catalytically similar to Pt and Ir, such as Ru and Pd, which are studied less extensively.[46–48]

Saturation coverages, however, have been shown to exceed unity on several metal catalysts, especially at low metal loadings; $\theta_{sat}$ values of 1.3–2.0, 1.2–1.98, and 1.24–3.0 have been reported for Pt,[49,50] Rh,[50,51] and Ir,[45,50] respectively, using TEM (for particles >0.6 nm) and XRD (for particles >5 nm). Extended X-ray absorption fine structure (EXAFS) is also used in conjunction with chemisorption measurements, which estimates particle size by measuring the average coordination number of metals within nanoparticles (which increases with increasing particle size);[52] $\theta_{sat}$ of 1.14 and 2.68 for Pt and Ir particles (<4 nm), respectively, have been reported by comparing EXAFS and $H_2$ chemisorption data.[50] These high $\theta_{sat}$ values have been attributed to H* spillover to the support (artificially inflating H:$M_s$ ratios),[53] H* diffusion into the bulk,[54] or to the ability of under-coordinated metal atoms present at the edges and corners of supported particles to bind more than one H*.[45,50,51] $Al_2O_3$-supported Pt, Rh, and Ir particles show different $\theta_{sat}$ values, and the $\theta_{sat}$ values for Ir/$Al_2O_3$ and Ir/$SiO_2$ are independent of the support,[50] both of which indicate that hydrogen spillover is an unlikely explanation for supra-monolayer coverages.[55,56] Subsurface hydrogen has been observed on Pd, which can form hydrides and act as a hydrogen storage medium.[57] The solubilities of H* into bulk Pt, Rh, and Ir, however, are low[58] and it is unlikely that significant amounts of subsurface H* exist in these materials. Recent DFT studies[15,59] and infrared experiments[60] for CO* chemisorption on Ru clusters confirm the formation of bridge-bound geminal dicarbonyl species on low-coordinated corner and edge atoms, which lead to supra-monolayer coverages (CO*:$Ru_s$ >1). An assumed $\theta_{sat}$ value of unity in chemisorption measurements could lead to underestimated particle sizes for metals that can reach supra-monolayer coverages because the larger $H_2$ uptake will be inaccurately attributed to a larger dispersion. A 1 nm Ir particle that can reach 2 ML coverage, for example, would be described as a 0.5 nm particle by chemisorption if a value of unity is used for $\theta_{sat}$.

Here, we use density functional theory calculations (DFT) to provide a quantitative description of how H* covers Ir and Pt nanoparticles ranging from 38 to 586 atoms (0.80–2.4 nm average diameter) by examining symmetrically-covered sub- and supra-monolayer H* adlayers at a wide range of coverages ($\theta_H$ = 0.09–3.63 ML). Our results indicate that under-coordinated edge and corner atoms, present on all clusters to different extents, uptake multiple H* atoms, leading to supra-monolayer coverages. H* prefers to adsorb to surface sites rather than subsurface sites even at very high coverages (1.84–3.63 ML, depending on particle size), ruling out H* ingression as an explanation for supra-monolayer coverages on Ir and Pt particles. This study attempts to establish correlations between saturation coverages and particles size that can be used to improve estimates of particle size from $H_2$ chemisorption.

## Methods

Periodic, planewave density functional theory (DFT) calculations were performed using the Vienna ab initio simulation package (VASP).[61,62] Planewaves were constructed using projector augmented-wave (PAW) potentials with an energy cutoff of 396 eV.[63–65] The revised Perdew−Burke−Ernzerhof (RPBE) form of the generalized gradient approximation (GGA) was used to describe exchange and correlation energies.[66,67] Wavefunctions were converged until electronic energies varied less than $10^{-6}$ eV. Forces on all atoms were determined using a fast Fourier transform (FFT) grid with a cutoff equal to twice the planewave cutoff and structures were geometrically optimized until the forces on all atoms were less than 0.05 eV Å$^{-1}$.

Gas-phase $H_2$ was modeled within an $18 \times 18 \times 18$ Å unit cell of empty space. Ir (111) and Pt (111) surfaces were modeled as $4 \times 4$ closed-packed periodic lattices with four layers orthogonal to the surface and 10 Å of vacuum separating slabs; the bottom two layers were fixed in their bulk positions and the top two layers were relaxed. A $3 \times 3 \times 1$ Monkhorst-pack sampling of the first Brillouin zone (k-point mesh)[68] was used during geometric convergence, and after geometric convergence, a single-point calculation with a $6 \times 6 \times 1$ k-point mesh was performed to determine the electronic energy.

Symmetric cubo-octahedral Ir and Pt particles (38–586 atoms, 0.80–2.4 nm diameter) were examined, which include sites with different metal-atom coordination (Figure 1). For particle calculations, the Brillouin zone was sampled only at the Γ-point. Cubo-octahedral particles consist of eight hexagonal (111) terraces and six square (100) terraces connected by edge and corner atoms. The sizes of these particles can be described by the length of the edges connecting adjacent (111) terraces ($h$) and by the length of the edges connecting adjacent (111) and (100) terraces ($s$). The surface composition and details of all particles examined in this study are shown in Table 1.

H* preferably binds in an atop position on low-index Ir and Pt surfaces[69,70] and metal atoms in the (111) and (100) terraces of these particles were modeled as either bare or occupied by a single atop H* atom ($t_{111}$ and $t_{100}$ in Figure 1). Edge atoms, which have lower coordination numbers (CN = 7), may bind up to 2 atop H* atoms ($e_{11}$ and $e_{10}$ in Figure 1); corner atoms (CN = 6) may bind up to 3 atop H* atoms ($c$ in Figure 1). The edges of these nanoparticles, as previously observed for CO* on Ru,[15,59,60] may also bind a H* atom in their bridging sites ($be$ in Figure 1). The total number of different H* configurations is computationally intractable as coverage increases up to and beyond 1 ML, even if only these sites are considered. Generally, in this work we calculate energies of fully symmetric H* adlayers, in which all sites of each type have equivalent H* occupancies. The particles were filled with H* to find the minimum energy pathway from a bare surface to a surface with three atop H* per corner, two atop H* per edge, one atop H* per terrace, and one bridging H* for every edge site (designated as "3c,2e,1t,1be" in this work, 1.84–3.63 ML depending on particle size). The average adsorption energy ($\Delta E_{avg}$) of all $n$ H* on a particle is defined as the energy to form the $n$-H*-covered particle from a stoichiometric amount of gas-phase $H_2$ and a bare surface

$$\Delta \overline{E} = \frac{E[nH^*] - 0.5n \cdot E[H_2] - E[M]}{n} \quad (1)$$

The average binding energy of adding an extra $x$ H* to a surface ($x$ >1) containing $n$ H* is defined as the average differential binding energy ($\Delta \overline{E}_{diff}$)
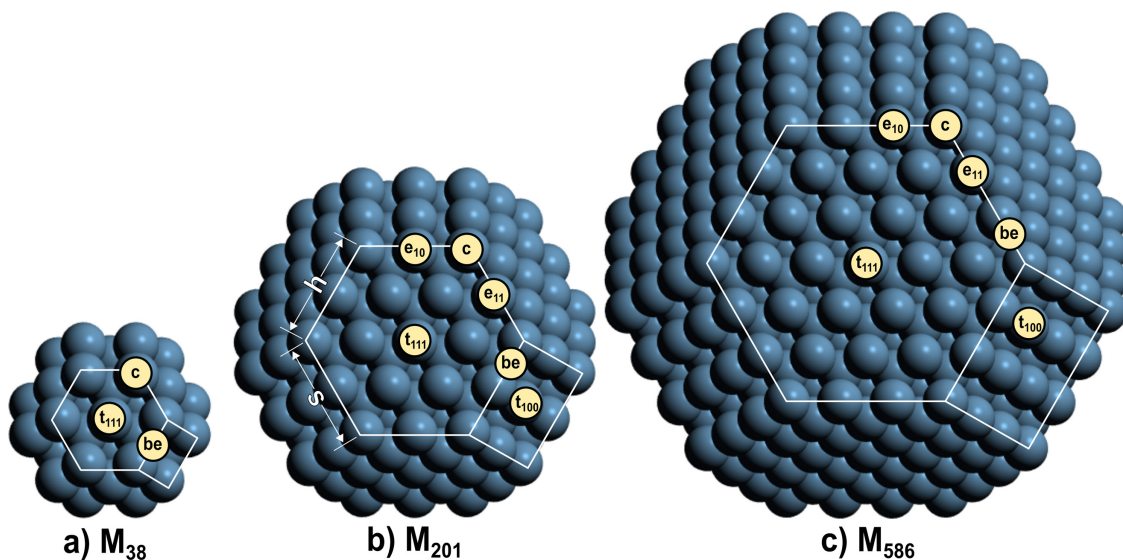
**Figure 1. Structural models of (a) M$_{38}$, (b) M$_{201}$, and (c) M$_{586}$ cubo-octahedral particles.**

The edges connecting adjacent (111) terraces and those connecting (111) and (100) terraces are described by *h* and *s*, respectively. Adsorption sites are labeled by $t_{111}$: (111) terrace, $t_{100}$: (100) terrace, *c*: corner, $e_{11}$: (111)–(111) edge, $e_{10}$: (111)–(100) edge, or *be*: bridge sites on the edges. White lines emphasize the exposed (111) and (100) planes. Figures depicting all other particles are shown in the Supporting Information (Figure S1). [Color figure can be viewed at wileyonlinelibrary.com]

$$\Delta \overline{E}_{diff} = \frac{E[(n+x)H^*] - 0.5x \cdot E[H_2] - E[nH^*]}{x} \quad (2)$$

If $x = 1$, then $\Delta \overline{E}_{diff}$ becomes the differential adsorption energy of an additional H* atom ($\Delta E_{diff}$). To assess the effects of H* coverage on edge/corner sites on the binding characteristics of terrace atoms, the adsorption energies of H* atoms centered on (111) terraces were computed (using Eq. 2). An extra H* atom was added to the "fully covered" particles (3c, 2e, 1t, 1be) to assess whether continued H* adsorption (if it occurred) would happen via H* migration into the bulk or via chemisorption on the surface.

## Results and Discussion

### Effect of binding mode and metal atom coordination number on H* binding energy

The adsorption energy of a single H* atom was calculated for different binding modes and locations, shown in Figure 2, to probe the effect of metal atom coordination on adsorption energies and determine where hydrogen would first adsorb on a bare particle. The cubo-octahedral metal particles expose atoms with four distinct coordination numbers (CN = 6, 7, 8, and 9), associated with exposed corners, edges, (100) terraces, and (111) terraces, respectively. Previous studies showed that on Ir and Pt(111) surfaces,[69,70] H* preferably binds atop metal atoms, which is confirmed here for the Ir$_{201}$ and Pt$_{201}$ particle (Figure 3); the binding energy for H* atop Ir (111) terraces is at least 10 kJ mol$^{-1}$ stronger than that for H* in threefold and bridging sites, and at least 8 kJ mol$^{-1}$ stronger on Pt (111) terraces. Therefore, only the atop binding mode was considered on the (111) terraces for all other particles.

There are six unique M$_s$ atoms on a M$_{201}$ cubo-octahedral particle (Figure 1b), which have six distinct atop sites (1 H–M bond), eight bridge sites (2 H–M bonds), six threefold sites (3 H–M bonds), and one fourfold site (4 H–M bonds) where H* can bind (Figure 2). The average H* binding energy on the Ir$_{201}$ particle is −42 kJ mol$^{-1}$ across all atop sites, −30 kJ mol$^{-1}$ across all bridge sites, −16 kJ mol$^{-1}$ across all three-fold sites, and −9 kJ mol$^{-1}$ at the fourfold site, showing a

**Table 1. Size and Surface Composition of all Metal Particles Examined in this Study**

| | | | $d_{avg}$ (nm) | | | | Terrace | | Edge | | Corner | Bridge-Edge | $\theta_{H^*}$ [d] |
| --- | --- | --- | --- | --- | --- | --- | --- | --- | --- | --- | --- | --- | --- |
| Size | | | | | | | $t_{111}$ | $t_{100}$ | $e_{11}$ | $e_{10}$ | *c* | *be*[c] | (ML) |
| $N$[a] | *h* | *s* | Ir | Pt | M$_s$[b] | Disp. | CN = 9 | 8 | 7 | 7 | 6 | 6.5 | max. |
| 38 | 2 | 2 | 0.80 | 0.82 | 32 | 0.84 | 8 | 0 | 0 | 0 | 24 | 36 | 3.63 |
| 79 | 3 | 2 | 1.11 | 1.13 | 60 | 0.76 | 24 | 0 | 12 | 0 | 24 | 48 | 2.80 |
| 116 | 2 | 3 | 1.28 | 1.31 | 78 | 0.67 | 24 | 6 | 0 | 24 | 24 | 60 | 2.69 |
| 124 | 3 | 2,3 | 1.34 | 1.37 | 84 | 0.68 | 32 | 4 | 8 | 16 | 24 | 60 | 2.57 |
| 201 | 3 | 3 | 1.59 | 1.62 | 122 | 0.61 | 56 | 6 | 12 | 24 | 24 | 72 | 2.28 |
| 314 | 4 | 3 | 1.91 | 1.94 | 174 | 0.55 | 96 | 6 | 24 | 24 | 24 | 84 | 2.03 |
| 405 | 3 | 4 | 2.09 | 2.13 | 204 | 0.50 | 96 | 24 | 12 | 48 | 24 | 96 | 2.00 |
| 586 | 4 | 4 | 2.40 | 2.45 | 272 | 0.46 | 152 | 24 | 24 | 48 | 24 | 108 | 1.84 |

[a]Total number of atoms.
[b]Number of exposed atoms on the surface.
[c]Number of bridging sites on the edges of the particle.
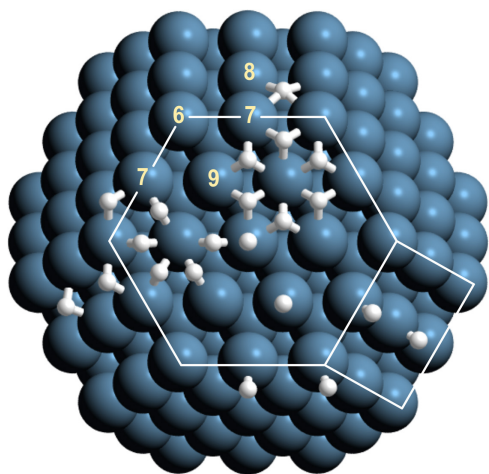[d]Maximum coverage (H*/M$_s$) examined in this study.

**Figure 2.** Distinct binding modes present on a $M_{201}$ cubo-octahedral particle (six atop sites, eight bridge sites, six threefold sites, and one fourfold site).

Labels denote the four distinct coordination numbers (CN = 6 – 9). White lines emphasize the exposed (111) and (100) planes. [Color figure can be viewed at wileyonlinelibrary.com]

general preference for H* to bind atop Ir as previously shown for (111) terraces.[69] Similarly for $Pt_{201}$, H* binds with an energy of −32, −30, −17, and −8 kJ mol$^{-1}$ at atop, bridging, threefold, and fourfold sites, respectively. For each type of binding mode (atop, bridging, threefold) on $Ir_{201}$, a clear trend exists between the average CN of the metal atoms at the site ($\overline{CN}$) and $\Delta E$ (Figure 3a). The weakening of M−adsorbates bonds with increasing metal coordination numbers was also observed in DFT studies of CO* chemisorption on Ru,[60] Pt,[71] and Au clusters,[72] and can be attributed to the back donation of electrons from the metal atoms to the adsorbed H*[73] or by simple bond-order-conservation concepts.[74] The most stable binding site for H* on $Ir_{201}$ is a bridge site between a corner and edge atom along the (111)–(100) edge ($\overline{CN} = 6.5$, $\Delta E = -58$ kJ mol$^{-1}$). H* binds atop the (111)–(100) edge (−46 kJ mol$^{-1}$) more strongly than it binds atop the (111)–(111) edge (−35 kJ mol$^{-1}$) despite those atoms having identical coordination numbers (CN = 7). Similarly, H* bridges atoms along the (111)–(100) edge (−58 kJ mol$^{-1}$) more strongly than it binds to bridge sites along the (111)–(111) edge (−38 kJ mol$^{-1}$, both sites $\overline{CN} = 6.5$). These differences

in binding energies for sites of identical $\overline{CN}$ demonstrate the inadequacy of coordination numbers as a descriptor for H* binding energies, as previously noted for CO* and O* on Au.[75] H* adsorption energies on $Pt_{201}$ change weakly with increasing $\overline{CN}$ (Fig. 3b) and the atop terrace (111) site is slightly more favorable (CN = 9, $\Delta E = -38$ kJ mol$^{-1}$) than other atop sites, in contrast to the strong trend with CN for atop-bound H* observed on $Ir_{201}$; despite these differences, H* is also most stable when bridging atoms along the (111)–(100) edge of $Pt_{201}$ ($\overline{CN} = 6.5$, $\Delta E = -45$ kJ mol$^{-1}$), similar to $Ir_{201}$. These results for $Ir_{201}$ and $Pt_{201}$ indicate that H* does not preferentially bind at threefold or fourfold sites; for other particle sizes, we focus on atop sites and bridging sites along particle edges.

Increasing or decreasing Ir particle size also affects H* binding energies, even for identical sites. $Ir_{38}$ particles bind H* very strongly compared to larger particles for all sites considered, while increasing the particle size from $Ir_{79}$ to $Ir_{586}$ slightly strengthens H* binding. For example, H* binds atop a corner atom with a binding energy of −63 kJ mol$^{-1}$ on an $Ir_{38}$ particle, but that weakens to −42 kJ mol$^{-1}$ on an $Ir_{79}$ particle, and then strengthens slightly to −50 kJ mol$^{-1}$ on an $Ir_{586}$ particle. This is consistent with previous reports that the adsorption energy of CO* on the atop site of the (111) terrace becomes weaker with increasing particle size from $Au_{13}$ to $Au_{309}$, above which particle size effects disappear and CO* adsorption energy becomes identical to that obtained from a periodic flat surface.[72] Here, the dramatic differences in binding energy between the $Ir_{38}$ and larger particles may be caused by nanoparticle effects in which small metal clusters (<40 atoms) cease to behave like the bulk metal as a result of the decrease in the valence and conductivity bands.[76] Overall, H* binds most strongly to bridge sites between two corner/edge atoms and most weakly atop a (111) terrace atom on all Ir particles studied. Increasing $\overline{CN}$ of the binding site weakens binding (Figure 5a), while increasing particle size slightly strengthens binding from $Ir_{79}$ to $Ir_{586}$, while H* binds most strongly to $Ir_{38}$ (Figure 4a).

H* binds strongly to the $Pt_{38}$ particle, but increasing Pt particle size has a less dramatic effect on $\Delta E$ values than is observed on Ir particles. $\Delta E$ is a weak function of particle size from $Pt_{79}$ to $Pt_{586}$ (Figure 4b). H*, for example, binds to the bridging site with −58 kJ mol$^{-1}$ in $Pt_{38}$ and that weakens to −45 kJ mol$^{-1}$ in $Pt_{201}$ then strengthens to −56 kJ mol$^{-1}$ in $Pt_{586}$. The binding energy of a terrace H* (CN = 9) weakens from −60 to −38 kJ mol$^{-1}$ with increasing particle size from $Pt_{38}$ to $Pt_{586}$, approaching the calculated value for Pt (111)
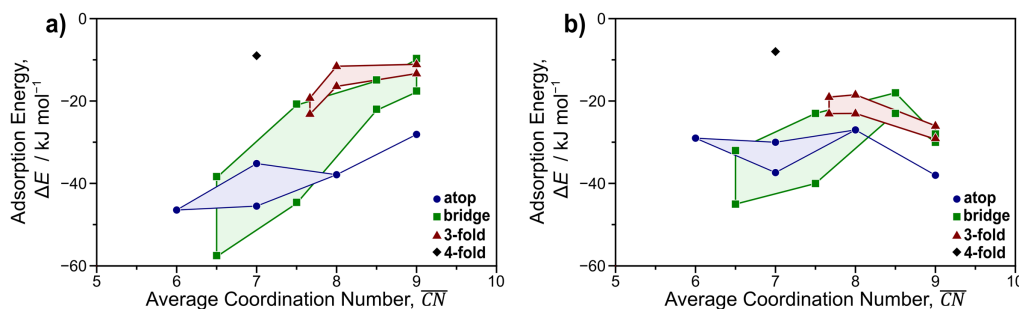


**Figure 3.** The adsorption energy of a single H* atom as a function of the average metal coordination number of the binding site on (a) $Ir_{201}$ and (b) $Pt_{201}$ particle.

Shadings are drawn to guide the eye to the overall trends between $\overline{CN}$ and $\Delta E$. [Color figure can be viewed at wileyonlinelibrary.com]
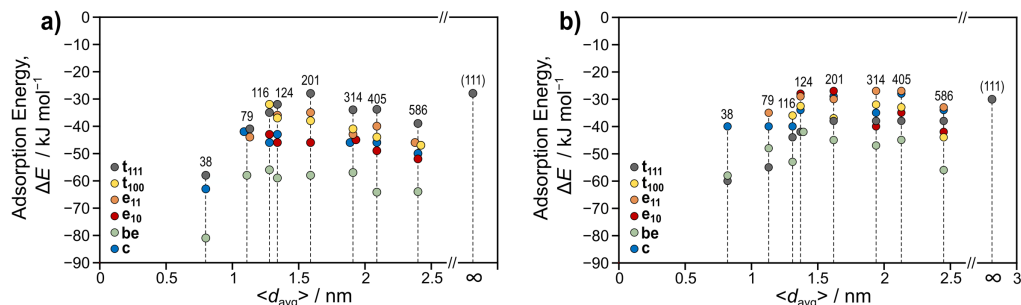
**Figure 4.** The adsorption energy of a single H* atom on different binding sites as function of particle size for (a) Ir and (b) Pt clusters.

[Color figure can be viewed at wileyonlinelibrary.com]

surface ($-30$ kJ mol$^{-1}$) (Figure 4b). Generally, Pt particles exhibit different trends than Ir particles (Figure 5); on Pt, H* adsorption on highly coordinated terrace (111) atoms is favorable and the coordination number has a weak effect on H* binding energy (Figure 5b).

*Covering the particles with H**

Here, we examine how H* covers Ir and Pt particles by systematically adding H* atoms to the particles as depicted in Scheme 1. As described in the second section, we consider up to three H* atop each corner atom, up to two H* atop each edge, up to one H* atop each terrace, and up to one H* bridging between each corner/edge atom. Chemisorbed species on metal clusters alter the binding properties of coadsorbates through a combination of through-space and through-surface interactions. Through-space interactions of H* atoms are expected to be weak because the Bohr radius of a hydrogen atom (0.0529 nm) is much smaller than the M–M bond distances of 0.27 and 0.28 nm for Ir and Pt, respectively, rendering direct through-space interactions implausible. Adsorbed H* atoms, instead, can interact locally through the metal surface by binding to the same metal atoms (metal-atom-sharing) or can interact nonlocally by electron withdrawing effects. Therefore, H* atoms adsorb on the surface in a manner that minimizes unfavorable interactions with coadsorbed species, as such, H* may partially cover bridging sites around the particle then start filling the terrace atoms to avoid metal-atom-sharing on bridge sites. Rigorous analysis of all possible

pathways to fill a bare particle is inefficient and computationally intractable; on a $M_{201}$ particle, for example, there are 21 distinct sites where the first H* atom can adsorb and 148 possible sites for the second atom, thus requiring a total of 3108 different calculations to rigorously determine the most favorable ground state of just a pair of H*. Our approach (Scheme 1) forces all sites of the same type to have the same H* occupancy, and provides a reasonable approximation of how H* fills metal particles without a prohibitive computational cost.

Figure 6 shows the differential adsorption energies as a function of coverage ($\theta$) for the most favorable pathways for all Ir and Pt particles. Differential H* binding energies ($\Delta E_{diff}$) increase gradually from $-29$ to $-19$ kJ mol$^{-1}$ with increasing coverage (from 1/16 to 1 ML) on a $4 \times 4$ Ir (111) surface; an additional H* (to 17/16 ML), however, binds much more weakly ($+4$ kJ mol$^{-1}$). For Pt (111), $\Delta E_{diff}$ weakens gradually from $-30$ kJ mol$^{-1}$ (1/16 ML) to $-9$ kJ mol$^{-1}$ at 1 ML and then to $+28$ kJ mol$^{-1}$ with the addition of an extra H* atom (17/16 ML). The dramatic increase in $\Delta E_{diff}$ at 1 ML and the positive $\Delta E_{diff}$ values at $>1$ ML suggest that H* coverage would not exceed 1 ML on a single crystal (111) terrace, consistent with earlier reports that show $\theta_{sat}$ is unity for single crystal (111) surfaces and large unsupported metal particles (which are comprised almost entirely of low-index terraces).[31,40] The critical H* adsorption energy ($\Delta E_{diff}^{crit}$) could therefore lie between $-9$ and $+4$ kJ mol$^{-1}$ based on calculated $\Delta E_{diff}$ values and prior observations that $\theta_{sat}$ is unity for (111) surfaces. The errors associated with DFT calculations of
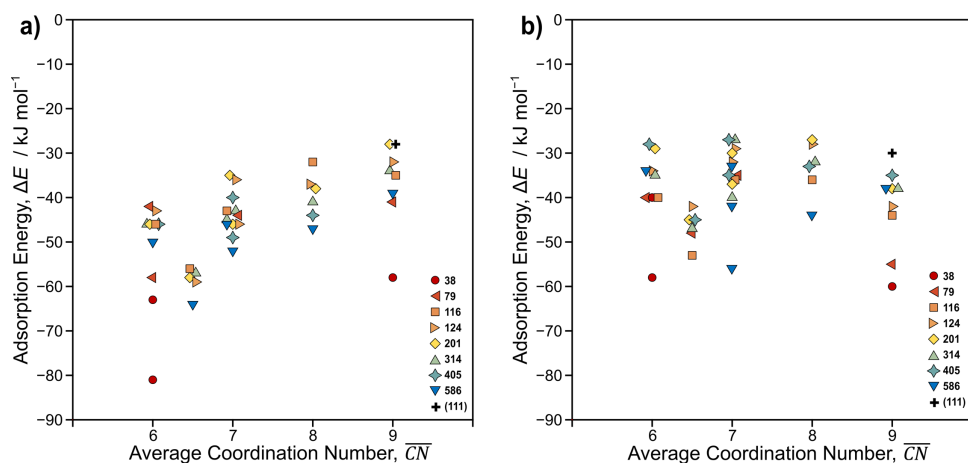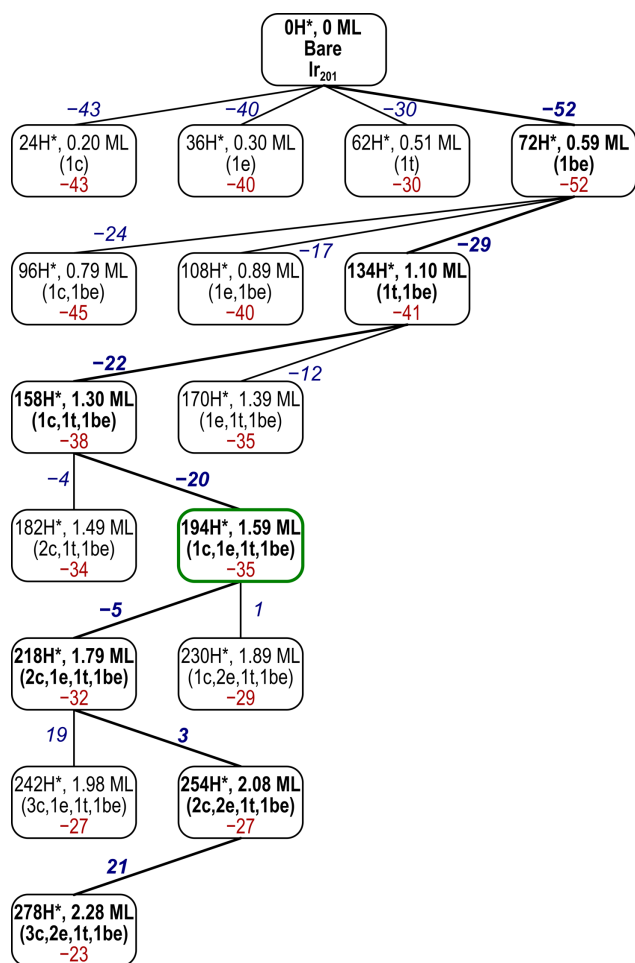


**Figure 5.** The adsorption energy of a single H* atom as a function of coordination number for (a) Ir and (b) Pt particles.

[Color figure can be viewed at wileyonlinelibrary.com]

**0H*, 0 ML**
**Bare**
**Ir_{201}**

*−43*    *−40*    *−30*    **−52**

| 24H*, 0.20 ML (1c) −43 | 36H*, 0.30 ML (1e) −40 | 62H*, 0.51 ML (1t) −30 | **72H*, 0.59 ML (1be)** −52 |

*−24*    *−17*    **−29**

| 96H*, 0.79 ML (1c,1be) −45 | 108H*, 0.89 ML (1e,1be) −40 | **134H*, 1.10 ML (1t,1be)** −41 |

*−22*    *−12*

| **158H*, 1.30 ML (1c,1t,1be)** −38 | 170H*, 1.39 ML (1e,1t,1be) −35 |

*−4*    **−20**

| 182H*, 1.49 ML (2c,1t,1be) −34 | **194H*, 1.59 ML (1c,1e,1t,1be)** −35 |

**−5**    *1*

| **218H*, 1.79 ML (2c,1e,1t,1be)** −32 | 230H*, 1.89 ML (1c,2e,1t,1be) −29 |

*19*    **3**

| 242H*, 1.98 ML (3c,1e,1t,1be) −27 | **254H*, 2.08 ML (2c,2e,1t,1be)** −27 |

**21**

| **278H*, 2.28 ML (3c,2e,1t,1be)** −23 |

**Scheme 1. The minimum energy pathway to fill the Ir_{201} particle (bold). Average H* binding energies ($\Delta \overline{E}$, red) and average differential binding energies ($\Delta \overline{E}_{diff}$, blue, bold, italics) are shown in kJ mol⁻¹.**

**Each state shows the number of H* atoms, the H* coverage, and the occupancy of corner (*c*), edge (*e*), terrace (*t*), and bridging-edge (*be*) H* sites. Similar schemes for the other Ir particles are shown in the Supporting Information (Schemes S1–S7). [Color figure can be viewed at wileyonlinelibrary.com]**

adsorption enthalpies and the entropies of adsorbed species prohibit us from using the adsorption free energy to predict saturation coverages, thus we assume here a $\Delta E_{diff}^{crit}$ value of −5 kJ mol⁻¹ for both Ir and Pt (and for all particle sizes). Neglecting these errors, one can estimate an adsorption free energy of 15 kJ mol⁻¹ for an adsorption enthalpy of −5 kJ mol⁻¹ by calculating the entropy of adsorbed H* using vibrational frequency analysis (S[H*] = 8 J mol⁻¹ K⁻¹) which gives an adsorption entropy of −67 J mol⁻¹ K⁻¹. This large, positive adsorption free energy would predict that the Pt and Ir (111) surfaces examined here do not reach saturation at near-ambient conditions (300 K, 100 kPa H_2), in direct contradiction with earlier reports. In fact, using these adsorption energies and vibrational frequencies to estimate S[H*] predicts that coverages never exceed 30% on Pt (111), also in stark contrast to earlier work. These adsorption energies are calculated using the RPBE exchange-correlation functional, which is known to underestimate binding energies (by 10–20 kJ mol⁻¹) compared to other functionals[77] and neglects attractive dispersive forces between coadsorbed species.[15] Furthermore, recent studies (García-Diéguez M, Hibbitts D, Iglesia E. Hydrogen chemisorption on Pt clusters at catalytic temperatures: Langmuir and two-dimensional gas models revisited. In preparation)[78] have demonstrated that vibrational frequency analysis can severely underestimate entropies of adsorbed species, such as H*. Taken together, these uncertainties and the results on Ir and Pt (111) surfaces suggest that an RPBE-calculated $\Delta E_{diff}^{crit}$ value of −5 kJ mol⁻¹ is a reasonable estimate of the weakest-bound H* that remains on the surface at the near-ambient conditions used in H_2 chemisorption.

Less than half of the Ir_{201} particle surface is made up of (111) terrace atoms, and the presence of undercoordinated edge and corner atoms significantly alters how adsorption occurs and at what coverage the particle surface is saturated in H* during H_2 chemisorption. Scheme 1 shows average binding energies of 24 H* adsorbed atop all corner atoms of Ir_{201} (1c, −43 kJ mol⁻¹), 36 H* atop all edge atoms (1e, −40 kJ mol⁻¹), 62 H* atop all terrace atoms (1t, −30 kJ mol⁻¹), and 72 H* bridging between corner/edge atoms (1be, −52 kJ mol⁻¹). The most favorable site to initially fill is therefore bridging between corner/edge atoms, as was the case for a single H* (–58 kJ mol⁻¹) (Figure 7a). Once these sites are filled, 24 H* can then bind atop all corners (1c,1be) with an average differential binding energy of −24 kJ mol⁻¹ (Eq. 2), 36 H* can bind atop all edges (1e,1be; −17 kJ mol⁻¹), and 62 H* can bind atop all terrace atoms (1t,1be; −29 kJ mol⁻¹), the last of which is most favorable (Figure 7b). At each state, we consider binding additional H* to each site (up to each site's limit) and we follow the path with the most favorable average differential binding energy (Scheme 1) until the particle has three H* atop every corner, two H* atop every edge, one H* atop every terrace, and one H* between every pair of corner and edge atoms (3c,2e,1t,1be) (Figure 7g). With increasing $\theta$, $\Delta \overline{E}_{diff}$ weakens, first from −52 kJ mol⁻¹ to −29 kJ mol⁻¹ at $\theta = 0.59$ ML, and then gradually to −20 kJ mol⁻¹ at 1.59 ML, before increasing more rapidly to 21 kJ mol⁻¹ at 2.28 ML. Coverages above 1.59 ML correspond to $\Delta \overline{E}_{diff}$ values ≥ −5 kJ mol⁻¹ ($\Delta E_{diff}^{crit}$) and are unlikely to occur at near-ambient conditions on the Ir_{201} particle because they will have large, positive adsorption free energies once zero-point and entropy effects are considered. Here, based on the assumed value for $\Delta E_{diff}^{crit}$ of −5 kJ mol⁻¹, we estimate 1.59 ML as the saturation coverage for Ir_{201} (Figure 7d), consistent with the reported supra-monolayer coverages on Ir.[45,50]

Smaller particles (Ir_{38–124}) fill with slightly different sequences than the Ir_{201} particle (Supporting Information Schemes S1–4), and these differences reflect the different number of sites of each type as the particle size varies. On the Ir_{38} particle, the eight terrace atoms are first occupied ($\Delta \overline{E}_{diff}$ = −69 kJ mol⁻¹), as they lack coadsorbate interactions, unlike the undercoordinated bridge sites that are filled next (36 H*, −46 kJ mol⁻¹). No edge atoms are present on M_{38} particles (all undercoordinated atoms are corners), and so the remainder of the particle is filled by sequential adsorption of H* to the 24 corner sites until all corners have three atop H* (3c, 1t, 1be). Adsorption above 2.88 ML ($\Delta \overline{E}_{diff}$ = +36 kJ mol⁻¹) is very unlikely at H_2 chemisorption conditions (Figure 6), indicating that Ir_{38} saturates at 2.88 ML (2c, 1t, 1be). For the Ir_{79–124} particles, $\Delta \overline{E}_{diff}$ values suggest that coverages saturate between 2 and 2.2 ML.
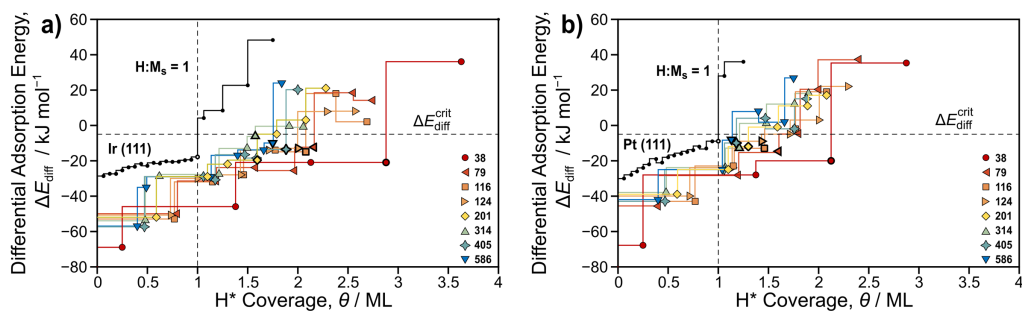
**Figure 6.** Average differential adsorption energies ($\Delta\bar{E}_{\text{diff}}$) for H* as a function of coverage ($\theta$) for all (a) Ir and (b) Pt particles.

[Color figure can be viewed at wileyonlinelibrary.com]

For large particles (Ir$_{314-586}$), similar to Ir$_{201}$, H* atoms first fill bridging sites between corner/edge metal atoms with $\Delta\bar{E}_{\text{diff}}$ values between $-54$ and $-57$ kJ mol$^{-1}$ (Supporting Information Schemes S5–7). Ir$_{314}$ particles reach a coverage of 1.56 ML (2c, 1e, 1t, 1be; $\Delta\bar{E}_{\text{diff}} = -7$ kJ mol$^{-1}$) before $\Delta\bar{E}_{\text{diff}}$ weakens to $-2$ kJ mol$^{-1}$ at 1.9 ML with the addition of an extra H* atom on the edges (2c, 2e, 1t, 1be), slightly above $\Delta E_{\text{diff}}^{\text{crit}}$ value. Ir$_{405}$ and Ir$_{586}$ particles saturate at 1.88 and 1.75 ML, respectively, reflecting the decrease in saturation coverages with increasing particle size as terrace (111) atoms dominate the surfaces; this decrease in saturation coverage is consistent with EXAFS-measured saturation coverages decreasing from 2.68 to 1.96 ML as particle size increased from 1.1 to 1.54 nm in diameter.[50] Saturation coverages are

shown in Figure 8 for selected particles and in Supporting Information Figures S9 and S10 for all other particles.

Pt particles saturate at lower coverages than Ir particles (Figure 6b), consistent with reported $\theta_{\text{sat}}$ values for these two metals with similar sizes.[45,50] The most favorable site to initially fill Pt$_{201}$ particle is the "be" site, as was the case for Ir$_{201}$, with an average binding energy of $-39$ kJ mol$^{-1}$ compared to $-34$, $-32$, and $-28$ kJ mol$^{-1}$ for 1t, 1e, and 1c, respectively. H* then binds to terrace atoms, then corners, then edges, before a second H* binds to edges, and finally a second H* binds to the corners (2c, 2e, 1t, 1be; 2.1 ML). Adding more H* atoms to the corners (3c, 2e, 1t, 1be; 2.28 ML) caused significant surface reconstruction, indicating that such coverages are unlikely to occur on Pt$_{201}$. Coverages above
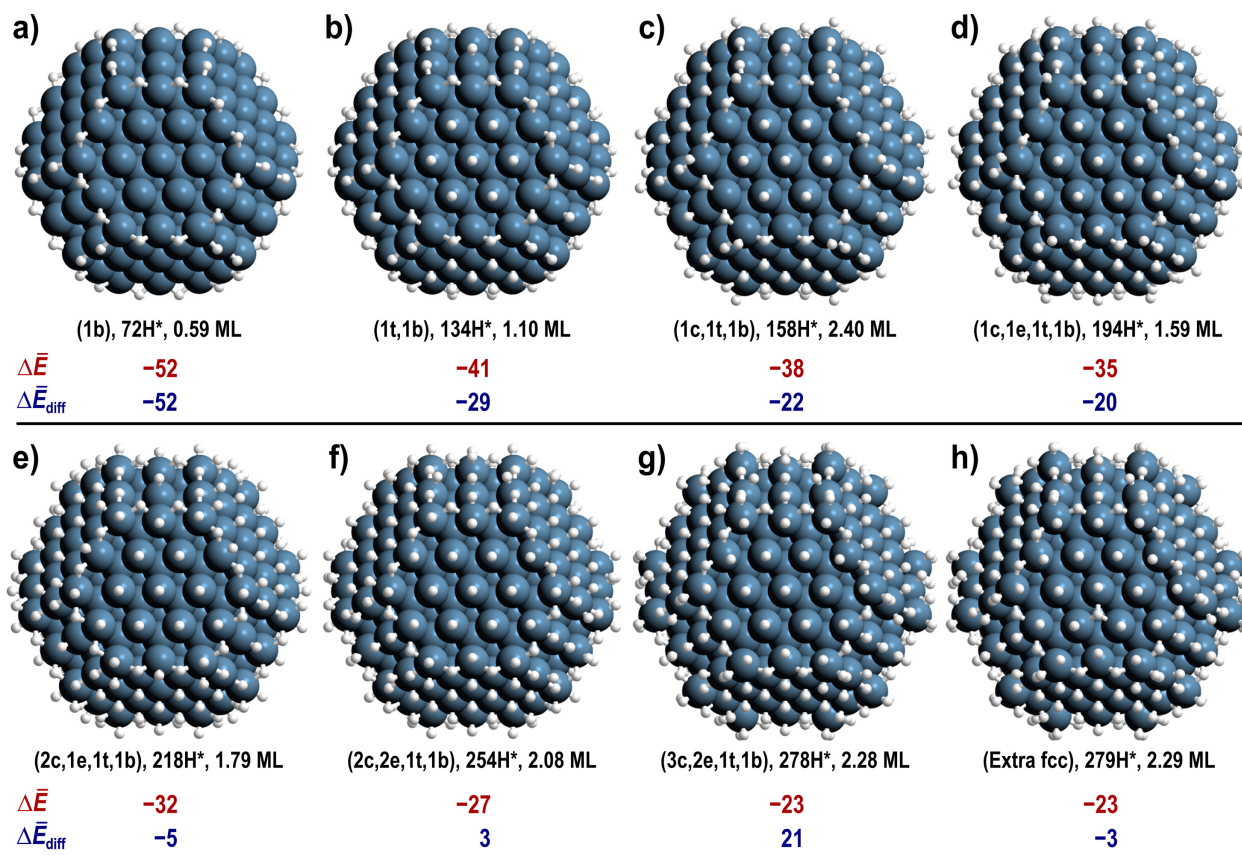


**Figure 7.** The minimum energy pathway of filling the Ir$_{201}$ particle.

Shown beneath each image are $\Delta\bar{E}$ (red) and $\Delta\bar{E}_{\text{diff}}$ (blue) in kJ mol$^{-1}$. Images of other Ir particles can be found in the Supporting Information (Figures S3–S8). [Color figure can be viewed at wileyonlinelibrary.com]
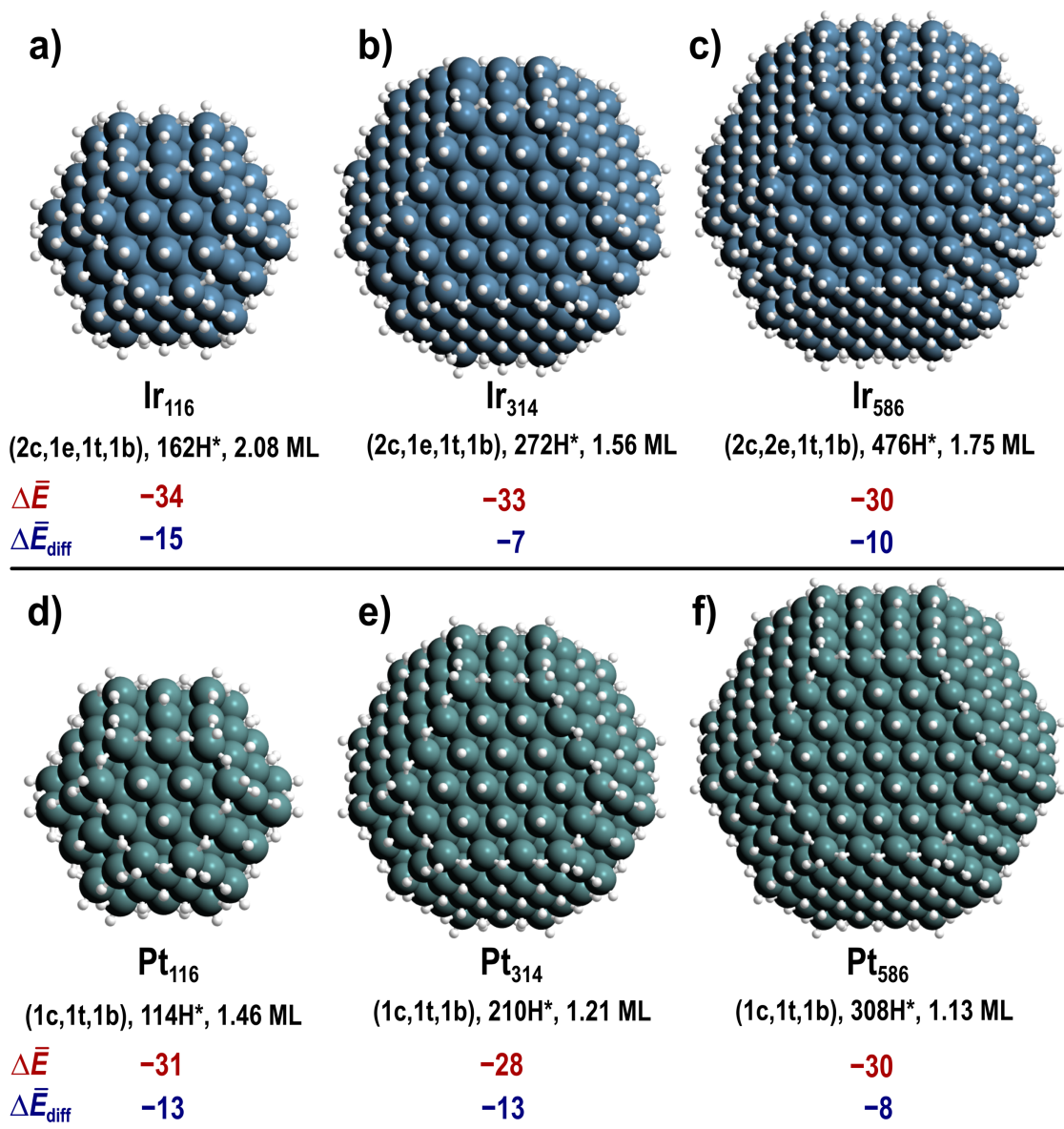
**Figure 8. Saturation coverages at $\Delta E_{diff}^{crit}$ for selected Ir (a–c) and Pt (d–f) particles.**

Shown beneath each image are $\Delta \bar{E}$ (red) and $\Delta \bar{E}_{diff}$ (blue) in kJ mol$^{-1}$. Images for all other particles can be found in the Supporting Information (Figures S9 and S10). [Color figure can be viewed at wileyonlinelibrary.com]

1.3 ML correspond to $\Delta \bar{E}_{diff}$ values $\geq -5$ kJ mol$^{-1}$ ($\Delta E_{diff}^{crit}$) and are unlikely to occur at near-ambient conditions, indicating that $Pt_{201}$ saturates at 1.3 ML while $Ir_{201}$ saturates at 1.79 ML, consistent with previous reports of higher coverages on Ir than on Pt.[45,50] Similar to $Ir_{38}$, terrace atoms are first filled in $Pt_{38}$ with an average binding energy of $-68$ kJ mol$^{-1}$ before H* atoms fill the bridging sites with $\Delta \bar{E}_{diff}$ value of $-28$ kJ mol$^{-1}$. H* is then added sequentially to the corners up to two H* atoms per each corner at 2.88 ML (2c, 1t, 1be; $\Delta \bar{E}_{diff} = +35$ kJ mol$^{-1}$) before surface reconstruction occurs at 3.63 ML (3c, 1t, 1be). $\Delta \bar{E}_{diff}$ values increase from $-20$ to $+35$ kJ mol$^{-1}$ at 2.13 ML, indicating that $Pt_{38}$ saturates at this coverage while $Pt_{116}$ and $Pt_{124}$ particles saturate at 1.46 and 1.43 ML, respectively. Large particles ($Pt_{314–586}$) reach saturation between 1.21 and 1.13 ML with one H* atom on bridge, terrace, and corner sites (1c, 1t, 1be).

High coverages of larger adsorbates, as reported previously for CO* on Ru nanoparticles,[15,59,60] increase the lateral compression of surface adlayers and weaken the bonds between adsorbed species and surface atoms, thus increasing the reactivity and desorption rate of bound species to create vacant sites required to adsorb reactants or dissociate species. Through-space coadsorbate interactions are, however, expected to be weak for small species like hydrogen but such species can also interact through the metal surface. The binding energy of a terrace H* atom changes weakly in Ir but more rapidly in Pt with increasing H* coverage on corner and edge metal atoms (see Supporting Information Section S5), indicating that local through-surface interactions are stronger in Pt than in Ir. Notably, the average surface metal-metal bond ($M_s$–$M_s$) distance increases with increasing H* coverage in Ir and Pt clusters, in contrast to single-crystal (111) surfaces (discussed in Supporting Information Section S6). These
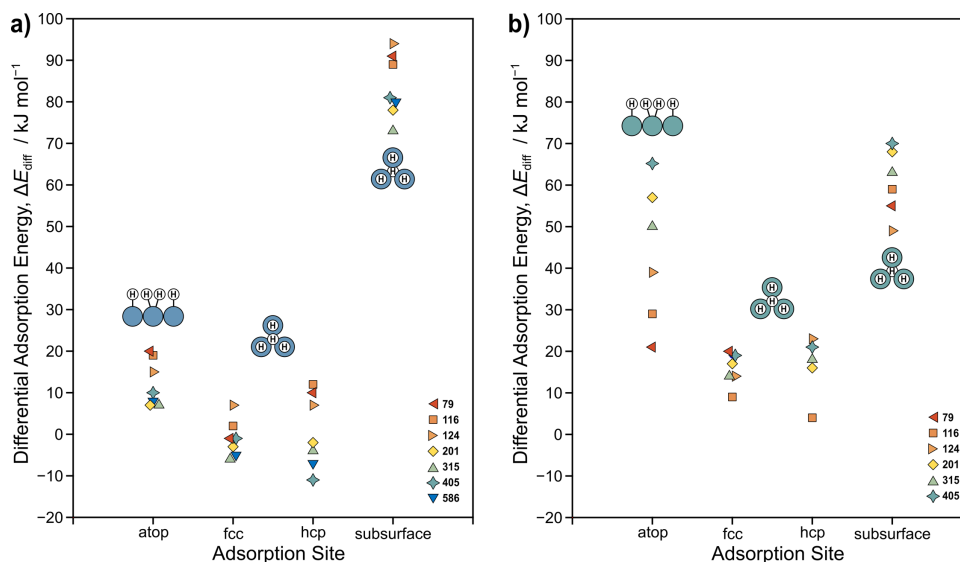
**Figure 9.** The adsorption energy of an extra H* atom above the fully covered state at different binding sites in (a) Ir and (b) Pt particles.

[Color figure can be viewed at wileyonlinelibrary.com]

relaxation effects with increasing coverage in metal clusters weaken $M_s$–$M_s$ bonds, leading to greater back-donation and stronger metal-adsorbate bonds.

### Adding an extra H* atom

An extra H* atom was added to the atop, threefold, or sub-surface sites in the terraces to examine the binding behavior of extra H* atoms above the "fully covered" states of Ir particles (3c,2e,1t,1be, 1.84–3.63 ML) and Pt particles (2c,2e,1t,1be, 1.75–2.88 ML) (Figure 9). The threefold sites preferentially bind the extra H* atom on larger particles with $\Delta E_{diff}$ from $-11$ to $+12$ kJ mol$^{-1}$ for Ir and from $+4$ to $+19$ kJ mol$^{-1}$ for Pt. Two H* atoms can also share a terrace metal atom in an atop binding mode with a less favorable $\Delta E_{diff}$ (Ir: $-8$ to $+20$ kJ mol$^{-1}$, Pt: $+21$ to $+65$ kJ mol$^{-1}$) than the threefold sites, on average. H* diffusion into a subsurface position (followed by readsorption of a surface H* atom) has much larger $\Delta E_{diff}$ values (Ir: $+73$ to $+94$ kJ mol$^{-1}$, Pt: $+49$ to $+70$ kJ mol$^{-1}$), indicating that the existence of subsurface H* atoms is unlikely, even at these extremely high surface coverages (1.75–3.63 ML).

### How supra-monolayer H* coverages affect chemisorption measurements of particle size

Dissociative chemisorption of $H_2$ is extensively used to estimate the dispersion and thus the crystallite size of metal catalysts dispersed on a support. Chemisorption measurements are especially important for highly dispersed catalysts because their size is difficult to measure using standard TEM instruments and XRD.[34] The measurement of the amount of chemisorbed H* at near ambient conditions gives the metal surface area and the metal dispersion for a known saturation coverage ($\theta_{sat}$). The metal dispersion $D$ is given by

$$D = \frac{2N_{H_2}}{N_M} \frac{1}{\theta_{sat}} \quad (3)$$

where $N_M$ and $N_{H_2}$ are the total number of moles of metal in the catalyst sample and $H_2$ chemisorbed (as 2 H*), and $\theta_{sat}$ is

the saturation coverage. Surface-averaged chemisorption diameters can be calculated from this dispersion as

$$d_{chem} = \frac{f_{shape}}{D} \frac{v_m}{a_m} \quad (4)$$

where $f$ is a particle shape correction factor (six for spherical particles), $v_m$ and $a_m$ are the volume and surface area of a metal atom. Typically, $\theta_{sat}$ is assumed to be unity during $H_2$ chemisorption experiments.

The number of H* atoms chemisorbed by a catalyst sample depends on the H*-content of many sites on, within, and off the metal cluster. For example, H* can exist within the bulk of metal nanoparticles, where $\theta_{bulk}$ is the fractional content (coverage) of bulk sites, whose number ($N_{bulk}$) is proportional to the volume of the particle (i.e., it is of $O(d^3)$). Similarly, we must account for H* adsorbed to terrace ($\theta_t N_t = O(d^2)$), edge ($\theta_e N_e = O(d^1)$), and corner ($\theta_c N_c = O(d^0)$) sites of the particle surface, as well as any possible H* spillover by including terms that account for H* adsorbed to the support near the metal-support interface ($\theta_{inter} N_{inter} = O(d^1)$) and away from that interface ($\theta_{supp} N_{supp} = O(d^0)$)

$$n_{sat} = \theta_{bulk} N_{bulk} \left(d^3\right) + \theta_t N_t \left(d^2, -d^1, d^0\right) + \theta_e N_e \left(d^1, d^0\right)$$
$$+ \theta_{inter} N_{inter} \left(d^1\right) + \theta_c N_c \left(d^0\right) + \theta_{supp} N_{supp} \left(d^0\right) \quad (5)$$

where the dependence of the number of each type of site on the particle diameter is given (e.g., the number of terrace atoms is given by a second-order polynomial). For large particles ($>6$ nm), the higher order terms will dominate this expression, and the H* content in the bulk and on the low-index terraces which prevail on such surfaces will dictate H* uptake values. Pt and Ir particles are not expected to form bulk H*, as indicated by the very low H* solubilities in those materials,[58] especially in contrast to Pd, which can form hydrides at reasonable conditions.[57] Here, we calculated differential adsorption energies for H* in bulk positions near surface atoms, and found very large, endothermic adsorption energies for all sizes of Ir and Pt particles examined, indicating that $\theta_{bulk} \approx 0$ for both materials (Figure 9). As described above, the dependence of $\theta_{sat}$ on the identity of the metal for Rh, Pd,

and Ir supported on $Al_2O_3$ and the independence of $\theta_{sat}$ for Ir supported on $Al_2O_3$ and $SiO_2$ suggest that H* spillover effects are minimal,[55,56] such that $\theta_{inter} \approx 0$ and $\theta_{supp} \approx 0$. The remaining terms of Eq. 5 represent H* adsorbed to surfaces, and for large particles, the H* coverage at terrace sites will dictate the overall H* uptake, and this explains the agreement between predicted and measured $\theta_{sat}$ values near unity for single crystal surfaces,[31,43] unsupported metal particles (>400 nm),[42] and large supported metal particles (>6 nm).[35–37,42–44] For smaller particles ($d \leq 6$ nm), however, the H* uptake on edges and corners cannot be neglected, and here we use the differential adsorption energies calculated for H* on surfaces of Ir and Pt particles (0.8–2.4 nm, Figure 6) to estimate the fractional coverages of such sites ($\theta_t$, $\theta_e$, and $\theta_c$) and to predict $\theta_{sat}(d)$, and we also discuss the errors associated with the common assumption of unity for $\theta_{sat}$.

Figure 6 shows, for multiple Ir and Pt particles, the coverage at which H* binds weaker than the $\Delta E_{diff}^{crit}$ value of $-5$ kJ mol$^{-1}$, which is our estimate of the weakest binding energy of H* that would adsorb at the near-ambient conditions used in the practice of H$_2$ chemisorption. This estimate is based on the calculated $\Delta E_{diff}$ values on Ir and Pt (111) surfaces, which are known to saturate at 1 ML, providing bounds ($-9$ and $+4$ kJ mol$^{-1}$) on $\Delta E_{diff}^{crit}$. Because it arises from the calculated $\Delta E_{diff}$ of a known surface, this estimate of $\Delta E_{diff}^{crit}$ does not require an accurate estimate of the entropy of adsorbed H* or of the systematic errors in $\Delta E_{diff}$ caused by our use of an "underbinding" exchange-correlation functional (RPBE) or by the lack of dispersive coadsorbate interactions in our DFT models. Estimated $\theta_{sat}$ values for Ir and Pt particles of increasing size are shown in Figure 10a, and as particle size increases to infinity, $\theta_{sat}$ approaches the saturation coverage of (111) terraces (1 ML). Correlations between $\theta_{sat}$ and $d_{real}$ for Ir and Pt particles, based on the saturation coverages at $\Delta E_{diff}^{crit} = -5$ kJ mol$^{-1}$, are given by

$$\theta_{sat} = \frac{\theta_t N_t(d^2, -d^1, d^0) + \theta_e N_e(d^1, d^0) + \theta_c N_c(d^0)}{N_{surf}(d^2)} \quad (6)$$

where the dependence of the number of each type of site on the particle diameter is given. From these expressions for the number of sites, we can get an expression for $\theta_{sat}$ that depends on the

coverage of terrace, edge (including bridging-edge sites), and corner atoms, and how much of the surface is occupied by each site $(f_i)$

$$\theta_{sat} = \theta_t(1 - f_e - f_c) + \theta_e f_e(d^{-1}, -d^{-2}) + \theta_c f_c(d^{-2}) \quad (7)$$

From this general formula, a semiempirical relationship can be described

$$\theta_{sat} = 1 + \alpha(d_{real}^{-1}) + \beta(d_{real}^{-2}) \quad (8)$$

where $\alpha$ is related to the excess coverage of edge H*, and $\beta$ relates to a weighted difference between the excess coverages of corner H* and edge-atop H* atoms. This equation can be used to fit the critical coverages estimated for Ir ($\alpha = 1.21$; $\beta = 0.203$) and Pt ($\alpha = 0.0364$; $\beta = 0.735$), and gives good agreement with those values, as shown in Figure 10a. These estimates of saturation coverage can be used to improve H$_2$ chemisorption analysis by substituting Eq. 8 into Eqs. 3 and 4

$$d_{chem} = \frac{N_M f_{shape}}{2N_{H_2}} \frac{v_m}{a_m} \left(1 + \alpha(d_{chem}^{-1}) + \beta(d_{chem}^{-2})\right) \quad (9)$$

Figure 10b shows the average diameters of all metal particles examined in this study compared to the particle sizes that would be estimated from H$_2$ chemisorption assuming a $\theta_{sat}$ of unity ($d_{unity}$). Particle sizes would be underestimated by a factor of 2–4 for $M_{38}$ particles (estimates of 0.2 nm for Ir and 0.4 nm of Pt compared to real sizes near 0.8 nm), whereas $M_{586}$ particle sizes (2.4 nm) would be underestimated by 43% for Ir (1.37 nm estimated) and 12% for Pt (2.16 nm estimated) if a $\theta_{sat}$ value of unity were used. Extrapolating our correlation (Eq. 9) to a 5 nm particle, we obtain $\theta_{sat}$ values of 1.25 for Ir and 1.04 for Pt, indicating that $d_{unity}$ would be 4 nm for Ir and 4.8 nm for Pt. These deviations depend not only on the size of the particle, but also on the metal because different metals have different affinities for H*, particularly at undercoordinated sites, and we are currently repeating this study on other transition metals to extend the correlations provided here (Eq. 8 and Figure 10) that can improve H$_2$ chemisorption measurements.
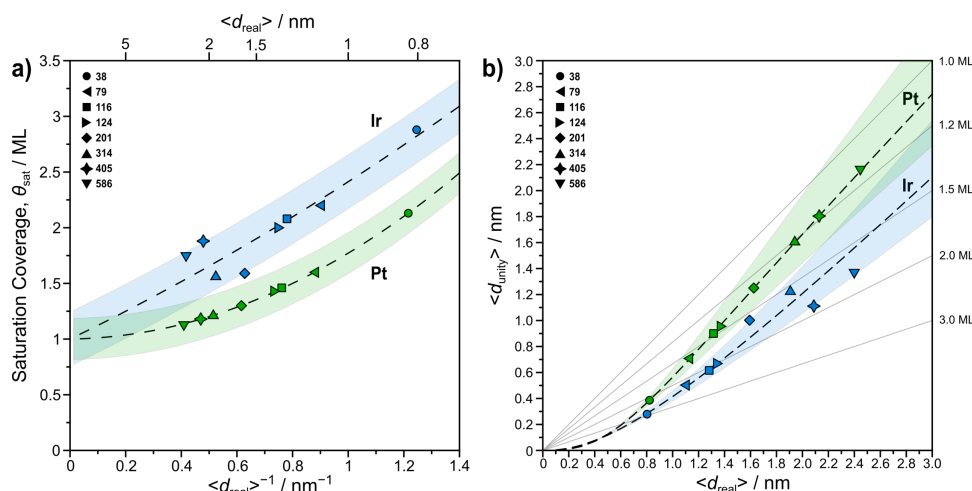


Figure 10. (a) Saturation coverages at $\Delta E_{diff}^{crit}$ as a function of particle size for Ir (blue) and Pt (green) particles. (b) Deviation of estimated particles size using chemisorption measurements from the actual size.

Dashed lines represent second-order fits using Eq. 8. Shadings represent 90% confidence intervals. [Color figure can be viewed at wileyonlinelibrary.com]

## Conclusions

Differential adsorption energies for H* chemisorption on Ir and Pt particles (38–586 atoms, 0.80–2.45 nm) were calculated using DFT by modeling systematic increases in H* coverage (up to 3.63 ML) to determine the origin of supra-monolayer coverages previously observed,[45,50] to estimate the saturation coverage ($\theta_{sat}$) of H* at the near-ambient conditions used in H$_2$ chemisorption measurements, and to evaluate the accuracy of the common assumption that $\theta_{sat}$ is unity for particle size estimates from H$_2$ chemisorption isotherms.

Sequential H* adsorptions on Ir and Pt (111) surfaces weaken gradually as coverage increases from 1/16 to 1 ML, and then dramatically with the addition of one more H* atom, indicating that H* coverage would not exceed 1 ML on a single crystal (111) terrace, confirming earlier reports.[31,40] The presence of undercoordinated edge and corner atoms in metal nanoparticles, however, significantly alters how particles fill and at what coverages they saturate. Undercoordinated metal atoms can accommodate multiple H* atoms giving rise to supra-monolayer coverages. $\Delta\overline{E}_{diff}$ values suggest that H* continues to adsorb beyond 1 ML and saturation coverages of up to 2.9 ML on Ir and 2.1 ML on Pt are plausible, consistent with prior experimental studies.[45,49,50] H* adsorption on surfaces remains more favorable than H* diffusion into the bulk at very large coverages (1.8–3.6 ML depending on the metal size), indicating that the existence of subsurface H* atoms is unlikely for Ir and Pt catalysts. Chemisorption measurements using an assumed H:M$_s$ of unity underestimate the particle sizes of highly dispersed particles by up to 75% (i.e., a 1 nm particle will appear to be 0.25 nm by H$_2$ chemisorption). This deviation decreases with increasing particle size as the highly coordinated terrace sites dominate the surfaces of large particles, but remains relevant even for 5 nm Ir particles (which would be estimated as 4 nm if $\theta_{sat}$ is assumed to be unity). Correlations are presented for Ir and Pt which give estimates of $\theta_{sat}$ as a function of particle diameter, and these can be used to improve particle size estimates from H$_2$ chemisorption by recognizing that multiple H* can adsorb to undercoordinated metal atoms that make up a significant fraction of the surface of highly dispersed metals.

## Literature Cited

1. Chorkendorff I, Niemantsverdriet JW. *Concepts of Modern Catalysis and Kinetics*. Weinheim, Germany: Wiley-VCH Verlag GmbH & Co. KGaA, 2003.
2. Bond GC. *Metal-Catalysed Reactions of Hydrocarbons*. New York: Springer, 2005.
3. Bond GC, Wells PB. The mechanism of the hydrogenation of unsaturated hydrocarbons on transition metal catalysts. *Adv Catal*. 1965; 15:91–226.
4. Shilov AE, Shul'pin GB. Activation of C−H bonds by metal complexes. *Chem Rev*. 1997;97(8):2879–2932.
5. Punniyamurthy T, Velusamy S, Iqbal J. Recent advances in transition metal catalyzed oxidation of organic substrates with molecular oxygen. *Chem Rev*. 2005;105(6):2329–2364.
6. Yao Y. The oxidation of CO and hydrocarbons over noble metal catalysts. *J Catal*. 1984;87(1):152–162.
7. Katzer JR, Sleight AW, Gajardo P, Michel JB, Gleason EF, McMillan S. The role of the support in CO hydrogenation selectivity of supported rhodium. *Faraday Discuss Chem Soc*. 1981;72:121.
8. Greeley J, Stephens IE, Bondarenko AS, Johansson TP, Hansen HA, Jaramillo TF, Rossmeisl J, Chorkendorff IN, Nørskov JK. Alloys of platinum and early transition metals as oxygen reduction electrocatalysts. *Nat Chem*. 2009;1(7):552–556.
9. Sato S, White JM. Photodecomposition of water over Pt/TiO$_2$ catalysts. *Chem Phys Lett*. 1980;72(1):83–86.
10. Bangala DN, Abatzoglou N, Chornet E. Steam reforming of naphthalene on Ni-Cr/al$_2$o$_3$catalysts doped with MgO, TiO$_2$, and La$_2$O$_3$. *AIChE J*. 1998;44(4):927–936.
11. Beltramini JN, Wessel TJ, Datta R. Kinetics of deactivation of bifunctional Pt/Al$_2$O$_3$–Cl catalysts by coking. *AIChE J*. 1991;37(6): 845–854.
12. Aghalayam P, Park YK, Vlachos DG. Construction and optimization of complex surface-reaction mechanisms. *AIChE J*. 2000;46(10): 2017–2029.
13. Butt JB. Progress toward the a priori determination of catalytic properties. *AIChE J*. 1976;22(1):1–26.
14. Goddard SA, Cortright RD, Dumesic JA. Deuterium tracing studies and microkinetic analysis of ethylene hydrogenation over platinum. *J Catal*. 1992;137(1):186–198.
15. Hibbitts DD, Dybeck E, Lawlor T, Neurock M, Iglesia E. Preferential activation of CO near hydrocarbon chains during Fischer–Tropsch synthesis on Ru. *J Catal*. 2016;337:91–101.
16. Logan MA, Somorjai GA. Deuterium isotope effects on hydrogenation of carbon monoxide over rhodium. *J Catal*. 1985;95(1):317–320.
17. Hibbitts DD, Jiménez R, Yoshimura M, Weiss B, Iglesia E. Catalytic NO activation and NO–H$_2$ reaction pathways. *J Catal*. 2014;319:95–109.
18. Tamm S, Olsson L, Fogel S, Gabrielsson P, Skoglundh M. A kinetic model of the hydrogen assisted selective catalytic reduction of NO with ammonia over Ag/Al$_2$O$_3$. *AIChE J*. 2013;59(11):4325–4333.
19. Hibbitts DD, Iglesia E. Prevalence of bimolecular routes in the activation of diatomic molecules with strong chemical bonds (O$_2$, NO, CO, N$_2$) on catalytic surfaces. *Acc Chem Res*. 2015;48(5):1254–1262.
20. Dahl S, Logadottir A, Egeberg RC, Larsen JH, Chorkendorff I, Törnqvist E, Nørskov JK. Role of steps in N$_2$ activation on Ru(0001). *Phys Rev Lett*. 1999;83(9):1814–1817.
21. Horiuti J, Polanyi M. Exchange reactions of hydrogen on metallic catalysts. *Trans Faraday Soc*. 1934;30:1164.
22. Sinfelt JH, Yates DJ. Catalytic hydrogenolysis of ethane over the noble metals of group VIII. *J Catal*. 1967;8(1):82–90.
23. Flaherty DW, Iglesia E. Transition-state enthalpy and entropy effects on reactivity and selectivity in hydrogenolysis of n-alkanes. *J Am Chem Soc*. 2013;135(49):18586–18599.
24. Flaherty DW, Hibbitts DD, Gürbüz EI, Iglesia E. Theoretical and kinetic assessment of the mechanism of ethane hydrogenolysis on metal surfaces saturated with chemisorbed hydrogen. *J Catal*. 2014; 311:350–356.
25. Flaherty DW, Hibbitts DD, Iglesia E. Metal-catalyzed C–C bond cleavage in alkanes: effects of methyl substitution on transition-state structures and stability. *J Am Chem Soc*. 2014;136(27):9664–9676.
26. Hibbitts DD, Flaherty DW, Iglesia E. Role of branching on the rate and mechanism of C–C cleavage in alkanes on metal surfaces. *ACS Catal*. 2016;6(1):469–482.
27. Hibbitts DD, Flaherty DW, Iglesia E. Effects of chain length on the mechanism and rates of metal-catalyzed hydrogenolysis of n -alkanes. *J Phys Chem C*. 2016;120(15):8125–8138.
28. Chia M, Pagán-Torres YJ, Hibbitts D, Tan Q, Pham HN, Datye AK, Neurock M, Davis RJ, Dumesic JA. Selective hydrogenolysis of polyols and cyclic ethers over bifunctional surface sites on rhodium–rhenium catalysts. *J Am Chem Soc*. 2011;133(32):12675–12689.
29. Koso S, Furikado I, Shimao A, Miyazawa T, Kunimori K, Tomishige K. Chemoselective hydrogenolysis of tetrahydrofurfuryl alcohol to 1,5-pentanediol. *Chem Commun*. 2009;(15):2035. doi:10.1039/B822942B
30. Pecoraro TA, Chianelli RR. Hydrodesulfurization catalysis by transition metal sulfides. *J Catal*. 1981;67(2):430–445.
31. Christmann K, Ertl G, Pignet T. Adsorption of hydrogen on a Pt(111) surface. *Surf Sci*. 1976;54(2):365–392.

32. Engstrom JR, Goodman DW, Weinberg WH. Hydrogenolysis of ethane, propane, n-butane, and neopentane on the (111) and (110)-(1x2) surfaces of iridium. *J Am Chem Soc*. 1988;110(25):8305–8319. (

33. Müller J. Selective chemisorption methods for the determination of the metal surface area in multicomponent catalysts. *Rev Pure Appl Chem*. 1969;19:151–165.

34. Sinfelt JH. Highly dispersed catalytic materials. *Annu Rev Mater Sci*. 1972;2(1):641–662.

35. Benesi H, Curtis R. Preparation of highly dispersed catalytic metals platinum supported on silica gel. *J Catal*. 1968;10(4):328–335.

36. Dorling TA, Eastlake MJ, Moss RL. The structure and activity of supported metal catalysts IV. Ethylene hydrogenation on platinum/silica catalysts. *J Catal*. 1969;14(1):23–33.

37. Wilson GR, Hall WK. Studies of the hydrogen held by solids. XVIII. Hydrogen and oxygen chemisorption on alumina- and zeolite-supported platinum. *J Catal*. 1970;17(2):190–206.

38. Bergeret G, Gallezot P. Particle size and dispersion measurements. In: G Ertl, H Knözinger, and J Weitkamp, editors. *Handbook of Heterogeneous Catalysis*. Weinheim, Germany: Wiley-VCH Verlag GmbH & Co. KGaA, 2008:738–765.

39. Whyte TE. Metal particle size determination of supported metal catalysts. *Catal Rev*. 1974;8(1):117–134.

40. Christmann K. Interaction of hydrogen with solid surfaces. *Surf Sci Rep*. 1988;9(1–3):1–163.

41. Brunauer S, Emmett PH, Teller E. Adsorption of gases in multimolecular layers. *J Am Chem Soc*. 1938;60(2):309–319.

42. Spenadel L, Boudart M. Dispersion of platinum on supported catalysts. *J Phys Chem*. 1960;64(2):204–207.

43. Renouprez A, Hoang-Van C, Compagnon PA. Supported platinum catalysts—small angle X-ray scattering and chemisorption. *J Catal*. 1974;34(3):411–422.

44. Freel J. Chemisorption on supported platinum II. stoichiometry for hydrogen, oxygen and carbon monoxide. *J Catal*. 1972;25(1):149–160.

45. McVicker GB, Baker RT, Garten RL, Kugler EL. Chemisorption properties of iridium on alumina catalysts. *J Catal*. 1980;65(1):207–220.

46. Brooks CS. Characterization of iridium catalyst surfaces by gas chemisorption. *J Colloid Interface Sci*. 1970;34(3):419–427.

47. Vannice M. The catalytic synthesis of hydrocarbons from $H_2$/CO mixtures over the group VIII metals I. The specific activities and product distributions of supported metals. *J Catal*. 1975;6(35):461.

48. Fiedorow RM, Chahar BS, Wanke SE. The sintering of supported metal catalysts II. Comparison of sintering rates of supported Pt, Ir, and Rh catalysts in hydrogen and oxygen. *J Catal*. 1978;51(2):193–202.

49. Sato S. Photoelectrochemical preparation of $Pt/TiO_2$ catalysts. *J Catal*. 1985;92(1):11–16.

50. Kip BJ, Duivenvoorden FBM, Koningsberger DC, Prins R. Determination of metal particle size of highly dispersed Rh, Ir, and Pt catalysts by hydrogen chemisorption and EXAFS. *J Catal*. 1987;105(1):26–38.

51. Wanke SE, Dougharty NA. Interaction of hydrogen, oxygen, and carbon monoxide with supported rhodium. *J Catal*. 1972;24(3):367–384.

52. Koningsberger DC, Prins R. *X-Ray Absorption: Principles, Applications, Techniques of EXAFS, SEXAFS, and XANES*. New York: John Wiley & Sons,1988.

53. Kramer R, Andre M. Adsorption of atomic hydrogen on alumina by hydrogen spillover. *J Catal*. 1979;58(2):287–295.

54. Yates JT, Peden CHF, Houston JE, Goodman DW. Subsurface penetration of chemisorbed hydrogen isotopes into the Ru(0001) crystal surface. *Surf Sci*. 1985;160(1):37–45.

55. Karim W, Spreafico C, Kleibert A, Gobrecht J, VandeVondele J, Ekinci Y, van Bokhoven JA. Catalyst support effects on hydrogen spillover. *Nature*. 2017;541(7635):68–71.

56. Prins R, Palfi VK, Reiher M. Hydrogen spillover to nonreducible supports. *J Phys Chem C*. 2012;116(27):14274–14283.

57. Behm RJ, Penka V, Cattania M-G, Christmann K, Ertl G. Evidence for "'subsurface'" hydrogen on Pd(110): an intermediate between chemisorbed and dissolved species. *J Chem Phys*. 1983;78(12):7486–7490.

58. McLellan R, Oates W. The solubility of hydrogen in rhodium, ruthenium, iridium and nickel. *Acta Metall*. 1973;21(3):181–185.

59. Liu J, Hibbitts D, Iglesia E. Dense CO adlayers as enablers of CO hydrogenation turnovers on Ru surfaces. *J Am Chem Soc*. 2017; 139(34):11789–11802.

60. Loveless BT, Buda C, Neurock M, Iglesia E. CO chemisorption and dissociation at high coverages during CO hydrogenation on Ru catalysts. *J Am Chem Soc*. 2013;135(16):6107–6121.

61. Kresse G, Furthmüller J. Efficient iterative schemes for ab initio total-energy calculations using a plane-wave basis set. *Phys Rev B*. 1996;54(16):11169–11186.

62. Kresse G, Furthmüller J. Efficiency of ab-initio total energy calculations for metals and semiconductors using a plane-wave basis set. *Comput Mater Sci*. 1996;6(1):15–50.

63. Kresse G, Hafner J. Ab initio molecular dynamics for liquid metals. *Phys Rev B*. 1993;47(1):558–561.

64. Kresse G, Hafner J. Ab initio molecular-dynamics simulation of the liquid-metal–amorphous-semiconductor transition in germanium. *Phys Rev B*. 1994;49(20):14251–14269.

65. Blöchl PE. Projector augmented-wave method. *Phys Rev B*. 1994; 50(24):17953–17979.

66. Kresse G, Joubert D. From ultrasoft pseudopotentials to the projector augmented-wave method. *Phys Rev B*. 1999;59(3):1758–1775.

67. Hammer B, Hansen L, Nørskov J. Improved adsorption energetics within density-functional theory using revised Perdew-Burke-Ernzerhof functionals. *Phys Rev B*. 1999;59(11):7413–7421.

68. Pack JD, Monkhorst HJ. Special points for Brillouin-zone integrations—a reply. *Phys Rev B*. 1977;16(4):1748–1749.

69. Krekelberg WP, Greeley J, Mavrikakis M. Atomic and molecular adsorption on Ir(111). *J Phys Chem B*. 2004;108(3):987–994.

70. Olsen RA, Kroes GJ, Baerends EJ. Atomic and molecular hydrogen interacting with Pt(111). *J Chem Phys*. 1999;111(24):11155–11163.

71. Allian AD, Takanabe K, Fujdala KL, Hao X, Truex TJ, Cai J, Buda C, Neurock M, Iglesia E. Chemisorption of CO and mechanism of CO oxidation on supported platinum nanoclusters. *J Am Chem Soc*. 2011;133(12):4498–4517.

72. Kleis J, Greeley J, Romero NA, Morozov VA, Falsig H, Larsen AH, Lu J, Mortensen JJ, Dułak M, Thygesen KS, Nørskov JK, Jacobsen KW. Finite size effects in chemical bonding: From small clusters to solids. *Catal Letters*. 2011;141(8):1067–1071.

73. Föhlisch A, Nyberg M, Hasselström J, Karis O, Pettersson LGM, Nilsson A. How carbon monoxide adsorbs in different sites. *Phys Rev Lett*. 2000;85(15):3309–3312.

74. Shustorovich E. The bond-order conservation approach to chemisorption and heterogeneous catalysis: applications and implications. *Adv Catal*. 1990;37:101–163.

75. Ma X, Xin H. Orbitalwise coordination number for predicting adsorption properties of metal nanocatalysts. *Phys Rev Lett*. 2017; 118(3):1–5.

76. Schmid G. Large clusters and colloids. Metals in the embryonic state. *Chem Rev*. 1992;92(8):1709–1727.

77. Wellendorff J, Silbaugh TL, Garcia-Pintos D, Nørskov JK, Bligaard T, Studt F, Campbell CT. A benchmark database for adsorption bond energies to transition metal surfaces and comparison to selected DFT functionals. *Surf Sci*. 2015;640:36–44.

78. Campbell CT, Sellers JRV. The entropies of adsorbed molecules. *J Am Chem Soc*. 2012;134(43):18109–18115.